

# A graph-mining algorithm for automatic detection and counting of embryonic stem cells in fluorescence microscopy images

Geisa M. Faustino<sup>a,\*</sup>, Marcelo Gattass<sup>a</sup>, Carlos J. P. de Lucena<sup>a</sup>, Priscila B. Campos<sup>b</sup> and Stevens K. Rehen<sup>b</sup>

<sup>a</sup>*Departamento de Informática, Pontifícia Universidade Católica do Rio de Janeiro, Rio de Janeiro, RJ, Brazil*

<sup>b</sup>*Instituto de Ciências Biomédicas, Universidade Federal do Rio de Janeiro, UFRJ, Rio de Janeiro, RJ, Brazil*

**Abstract.** Many cell-based research studies require the counting of cells in order to understand and validate experiments through statistical analyses. Although progress in imaging technology has enabled the automation of cell counting for many different cell types, this process still has to be done manually in the case of images of embryonic stem cells. In this paper, we present a new automatic algorithm to detect and count embryonic stem cells in fluorescence microscopy images that identifies pluripotent stem cells cultured *in vitro*. Our approach uses luminance information to generate a graph-based image representation. The cell pattern is defined as a subgraph, and a graph-mining process is applied to detect the cells. The method is tolerant to variations in cell size and shape. Moreover, it can easily be parameterized to handle different image groups resulting from distinct differentiation protocols. The paper presents numerical results from tests made on a database with more than two hundred images, including EB cryosection, embryoid body cell migration, murine embryonic stem cell colonies under murine embryonic fibroblast, and neurosphere images. The results from our algorithm were validated by expert biologists, and provide good precision, recall and F-measure. Finally, a comparative study with the widely used watershed algorithm is presented.

**Keywords:** Automatic cell counting, fluorescence microscopy image, graph-based image representation, graph mining, graph clustering

## 1. Introduction

Researchers have been developing a number of new techniques and software applications for biological and medical health care purposes [18,19,22,32,40,41]. Recent efforts have focused on eliminating subjectivity, accelerating processes such as cell counting or micro-calcification detection, and helping physicians improve their daily practice, make accurate diagnosis, and prevent diseases.

Embryonic stem (ES) cell is the term used to define cells that have unlimited proliferation and can originate

any kind of cell in an organism. Since ES cells were discovered, the possibility of using them to treat a variety of diseases has encouraged many research projects in biomedical areas. Because of their pluripotency property and the possibility to direct their differentiation *in vitro* to specific cell types, ES cells have become an alternative for cell-based treatments of various diseases, such as diabetes, Parkinson's, stroke, heart disease, and spinal cord injury, among others.

Cell counting plays an important role in statistical analysis and allows specialists to understand and validate experiments. When cells are stained properly, visual analysis can reveal biological mechanisms. Using different cell markers, researchers are able to determine, for instance, the total number of cells, how many have become specialized mature cells, and how many cells died. Although progress in imaging technology

---

\*Corresponding author: Geisa M. Faustino, Departamento de Informática, Pontifícia Universidade Católica do Rio de Janeiro, Rio de Janeiro, RJ, Brazil. E-mail: gfaustino@inf.puc-rio.br.

has enabled the automation of cell counting for many different cell types, in the case of ES cell images this process is still performed manually by expert biologists through visual inspection.

Monitoring the proportion of undifferentiated cells during culture is important to ensure the quality of the culture, and, as a result, the pluripotency of ES cells. However, manual counting is tedious and time-consuming, and its subjective nature can lead to a wide variation in the results. In practice, counting large amounts of cells manually leads to high standard deviations, yielding poor results. Thus, there is a clear need for an automatic method that is able to detect and count these cells. Such method can also be a useful tool for streamlining the evaluation of culturing methods and consequently accelerating stem cell therapy processes.

In this paper, we present a graph-mining algorithm to automatically detect and count ES cells in fluorescence microscopy images. This article is an extended version of a previous work [13]. Here, the proposed method is presented in detail to allow a better understanding of the strategy used to provide tolerance to changes in the size and shape of the cells, which can occur in normal laboratory procedures. We also show new results achieved by our algorithm, including two new types of captured images: murine embryonic stem (mES) cell colonies under murine embryonic fibroblast (MEF), and neurospheres. All the results presented here were visually validated by expert biologists and provide good precision, recall and F-measure. A comparative study with the widely used watershed algorithm is presented as well. To further support our research, we developed a free software application that implements our methodology, which was made publicly available on the web together with the images shown here. This software is already being used by expert biologists at the Institute of Biomedical Sciences at Federal University of Rio de Janeiro (UFRJ) in Brazil.

The remainder of the paper is organized as follows: Section 2 highlights some related studies; Section 3 describes image features and the acquisition process; Section 4 provides an overview of the method; Section 5 presents and discusses the experimental results; and Section 6 presents our conclusion and some future work.

## 2. Related work

In this section we briefly discuss some of the related works that are most relevant to our approach.

The technique most frequently used to detect differentiated cells is flow cytometry [17,34]. This technique can identify and quantify a large number of cells in a short period of time. Its results express the percentage of one or more types of cells within a population. However, this procedure is expensive and requires a trained technical specialist. Another disadvantage is the loss of spatial information, since this procedure can be applied only to cell suspension cultures. Thus, it is generally used as a complement to microscopy analysis, providing information about tissue architecture and cell localization as well as distribution of cellular fluorescence.

A number of researchers have been dealing with cell segmentation and counting in microscopy images [1,8,9,15,28,35,38]. Techniques based on machine learning [29,37,39] and on classical segmentation methods such as threshold, morphological filtering and watershed transformation [3,10,11,27] have been developed. However, these techniques do not address properly a problem that frequently occurs when the cells are partially or totally fused, as illustrated in Fig. 1a.

Since the discovery of the potential of stem cells, many researchers have been investigating the segmentation, tracking and quantification of these kinds of cells [2,7,16,20,21,24,25]. Althoff et al. [20] and Tang et al. [7] proposed methods for the segmentation and tracking of neural stem (NS) cells. Both approaches are based on classical segmentation methods and use information about the previous position of cells to decide which blobs correspond to real cells. Korzynska [2] presented a method for the automatic counting of NS cells growing in cultures which is performed in two steps: 1) the image is segmented into several regions; and 2) each homogeneous region is counted separately. Kachouie et al. [24–26] proposed methods to locate and track individual hematopoietic stem (HS) cells. In their first work [24], the authors proposed a deconvolution method in the form of an optimized ellipse fitting algorithm to locate individual HS cells. In subsequent articles [25,26], cell morphology information (e.g. cell size, boundary brightness, interior brightness and boundary uniformity or symmetry) is used to locate and track HS cells. However, all of these methods can handle only one type of stem cell in the images. In addition, since they tend to use morphological information or a traditional segmentation approach, they do not address properly the variations in cell size or shape.

Restif [6] proposed a method for the segmentation and evaluation of fluorescence microscopy images which was designed to handle nuclei and chromosomal

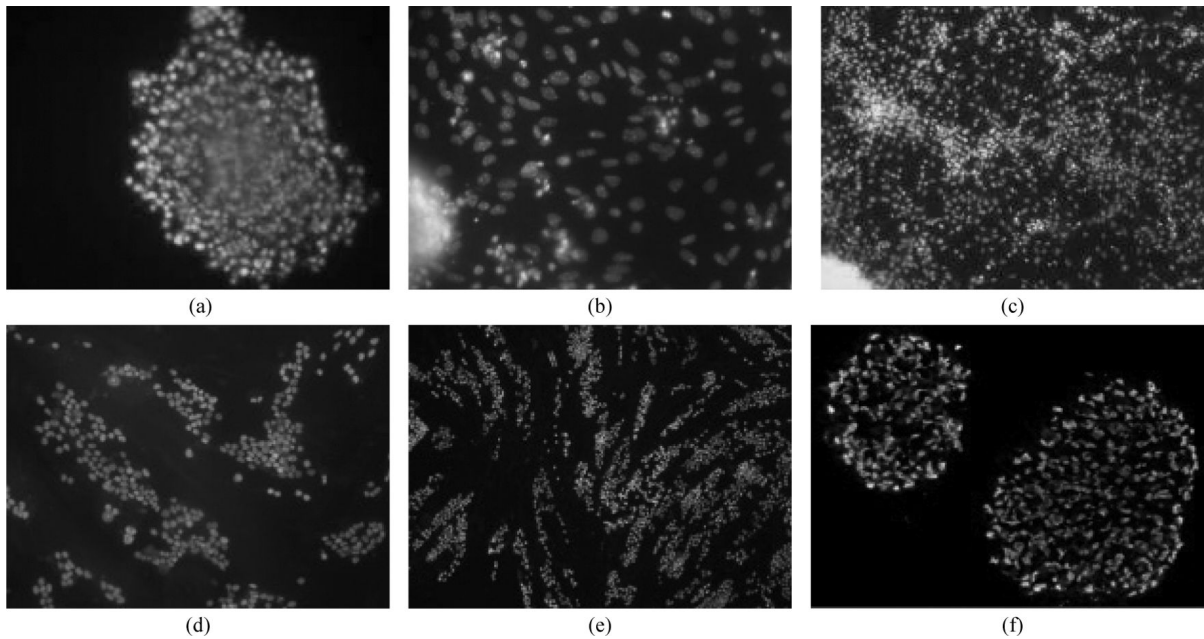


Fig. 1. Captured ES cell images: (a) EB cryosections; (b) and (c) EB cell migration with a  $40\times$  and  $20\times$  zoom, respectively; (d) and (e) images of mES cells under MEF with a  $20\times$  and  $10\times$  zoom, respectively; and (f) neurospheres.

probes. Nuclei segmentation is based on a parametric model of the histogram image. To detect the chromosomal probes, a dome-detection algorithm is used. A mask of fixed size, centered on a local maximum, is used to evaluate and classify the region as a dome or as noise according to a defined criterion.

Graphs are flexible and a powerful representation that has been applied successfully in computer vision, pattern recognition and related areas. Methods that use a graph-based approach to image segmentation have been proposed [5,30,31,36]. However, in the case of images where the objects are very clustered or clumped and with low-contrast boundaries (see Fig. 1a), these methods are not able to detect individual objects.

The first method dealing with several types of pluripotent stem cells in the same microscopy image was proposed by Faustino et al. [14] and was designed for images of stem cell sections from embryoid bodies (EB cryosection images). It uses luminance information to generate a graph-based image representation. The cell pattern is defined as a subgraph, and a graph-mining process is used to detect the cells.

Although this method works well, its performance is significantly reduced in images where there is more than one bright point per cell. In order to solve this shortcoming, an extended method was presented [13]. It incorporates a graph-clustering algorithm subsequent to the mining process, increasing the precision for im-

ages of EB cryosections and making the method suitable for images of migration of embryoid body cells with a  $40\times$  zoom.

The method proposed here uses the same idea presented by Restif [6]. The cells are represented by domes and a detection algorithm is used. However, we use a graph-based approach and do not have any previous information about cell shape. The advantages of this approach include its tolerance to variations in cell size or shape and its easy tuning for different image groups resulting from distinct differentiation protocols. Moreover, differently from previous works, our method can handle overlapping or highly clustered cells, such as the ones shown in Fig. 1a.

### 3. Image characterization

All images used in this work were collected by the Institute of Biomedical Sciences at UFRJ university in Brazil. There are images of stem cell sections from embryoid bodies (EB cryosections), neurospheres, embryoid body (EB) cell migration, and murine stem (mES) cell colonies under murine embryonic fibroblast (MEF). The protocols used and the acquisition system are described in the following sections.

### 3.1. EB cryosection images

Most differentiation protocols for ES cells involve the use of the embryoid body (EB) model. EBs are spherical structures obtained from ES colonies and cultured under non-adherent conditions. EBs are composed of cells from three germ layers (ectoderm, mesoderm and endoderm), and can be used in many differentiation protocols.

EBs are cultured for eight days through a neural differentiation process. In this procedure, the EBs are stimulated to differentiate into a neural phenotype through incubation during the last four days with retinoic acid at a final concentration of 2  $\mu$ M.

In order to obtain the EB cryosection images used here, a fraction of the EBs was fixed and processed for cryoprotection. Slices were prepared on cryostat to discern the number of individual cells in each embryoid body. The slice thickness used was 10  $\mu$ m, which corresponds to the average size of the nuclei. Next, the slices were incubated for 5 minutes with 4'-6-diamidino-2-phenylindole (DAPI), which is a nuclear counterstain. It binds to cell DNA and makes it visible in blue/cyan when visualized through fluorescence microscopy, as illustrated in Fig. 1a.

### 3.2. Neurosphere images

The acquisition of neurosphere images (Fig. 1f) is the same as for EB cryosections. Despite the similarity with EBs, neurospheres are floating spheres that enclose only neural progenitor cells.

### 3.3. Images of embryoid body cell migration

Images of embryoid body (EB) cell migration (Figs 1b and 1c) were obtained from another EB fraction, which was plated onto laminin/fibronectin-coated glass slides for four days to promote cell migration. Cells were fixed with 4% paraformaldehyde and stained as described previously.

### 3.4. Images of murine embryonic stem cell colonies under murine embryonic fibroblast

Images from murine embryonic stem (mES) cell colonies (Figs 1d and 1e) were obtained after immunocytochemistry assay. ES cells were cultured in inactivated murine embryonic fibroblast (MEF) and, on the fourth day, fixed onto coverslips using 4% paraformaldehyde. Next, for immunofluorescence de-

tection, the cells were incubated overnight with primary antibodies against Octamer-4 (Oct-4).

The transcription factor Oct-4 is an important protein for the self-renewal of ES cells, and its expression decreases during the differentiation process. Therefore, it is frequently used as a marker for undifferentiated cells.

After this period, the cells were incubated with secondary antibodies combined with fluorescent molecules (Alexa Fluor 546) for one hour, followed by five minutes of DAPI incubation.

### 3.5. Acquisition system

The acquisition system consisted of a Nikon Eclipse TE300 inverted epifluorescence microscope, a MagnaFire Digital CCD camera, and the Image Pro Express software. The acquisition procedure is semi-automatic and the specialist controls some parameters, such as magnification, exposure time and focus. The resolution of the captured images is fixed at  $1392 \times 1040$  pixels. A  $40 \times$  zoom was used for images of EB cryosections and neurospheres. The images of EB cell migration were captured using a  $40 \times$  and  $20 \times$  zoom. For images of mES cell colonies under MEF, a zoom factor of  $20 \times$  and  $10 \times$  was used. All images were stored using the Tagged Image File (.tif) format with lossless LZW compression.

## 4. Overview of our method

The proposed method is based on an important characteristic of images of ES cells: generally, each cell has one bright central point, and the luminance decreases monotonically from the bright point towards the cell border. Cell images captured with large zoom factors, such as  $40 \times$ , sometimes display additional bright points in their interior. Figure 3 illustrates the luminance as the elevation of a surface. In this interpretation each cell is identified as a dome. When a cell has more than one bright point, its dome top presents some local variations.

Our method is composed of six steps: five required steps (preprocessing, histogram partition, connected component detection, graph construction, and graph mining) and an optional step (graph clustering) to deal with the case of multiple bright points. Figure 2 provides an overview of the proposed method.

The preprocessing step consists basically in the application of a Gaussian filter to reduce noise. The goal

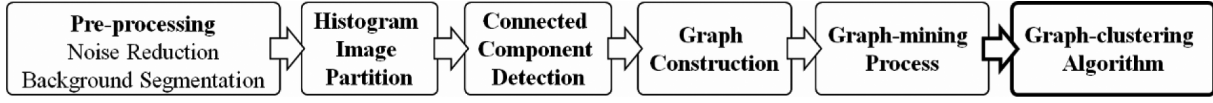


Fig. 2. Overview of the proposed method: each step is denoted by a box. The last box represents an optional step that can be added to the process in order to deal with the case of multiple bright points.

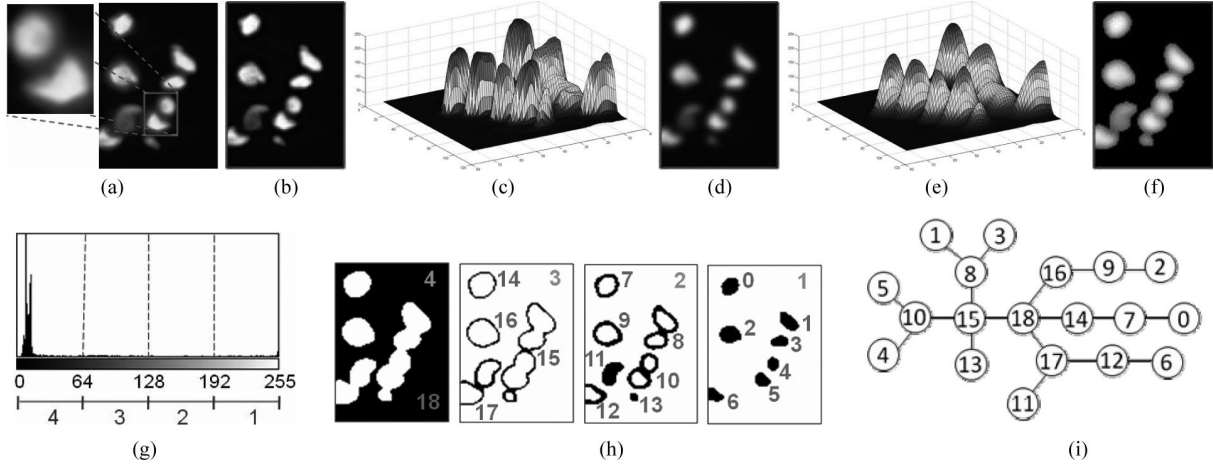


Fig. 3. Cell pattern and algorithm steps: (a) input image (EB cryosection); (b) luminance information; (c) the corresponding topological surface; (d) and (e) result of Gaussian blur filter – note that each cell is represented on the surface by a dome; (f) outcome of background segmentation; (g) histogram image and its partition in intervals of size  $\varepsilon = 64$ ; (h) the 8-connected components and the corresponding labels (in gray) for each interval; and (i) the graph-based image representation – note that the nodes with smaller index appear in the extremity of the graph.

is to reduce the number of false peaks without blurring or merging different cells into one. Note that, when the image presents cells with more than one bright peak, this step rarely merges them. These additional peaks will be treated by the last step of the algorithm. Figures 3c and 3e show the result of the Gaussian filter.

Since the images are captured in a controlled environment, the ES cells in these images can be separated from the background using a simple global threshold  $t = \mu + x\delta$ , where  $\mu$  is the mean value of the image,  $\delta$  is the standard deviation of the image, and  $x$  is a constant defined experimentally. The final part of the preprocessing step is to zero the intensity below the threshold  $t$ . Figure 3f and Fig. 4 illustrate this process.

In the second step of the algorithm, the horizontal axis of the image histogram is partitioned into intervals with fixed size ( $\varepsilon$ ). Figure 3g shows this partition with a size of 64 used only for illustration purposes. The actual partition size must be smaller, as presented below. Each partition defines a luminance class.

In order to detect the connected components (third step), the foreground image is partitioned into 8-connected regions of pixels that belong to the same luminance class. A 4-connected neighborhood can also be used, but it increases the size of the resulting graph.

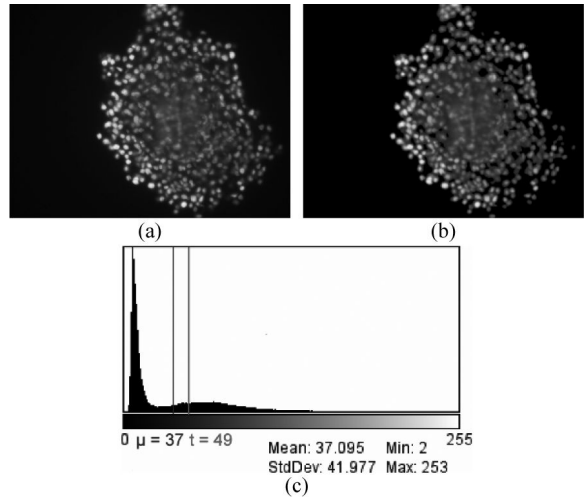


Fig. 4. Background segmentation step: (a) luminance information from image shown in Fig. 1a; (b) outcome of background segmentation; and (c) the histogram image with the corresponding values for  $\mu$  and  $t$ .

Next, the regions are labeled with natural consecutive numbers so that regions with higher luminance are attributed smaller numbers (see Fig. 3h). The result of this step is a matrix  $M$  with the same dimensions as

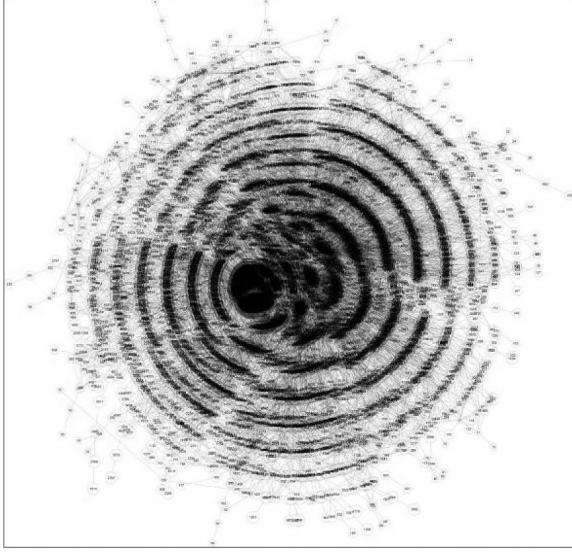


Fig. 5. An example of a typical graph: the graph-based representation of the image shown in Fig. 1a with a partition size of  $\varepsilon = 8$ . Note that the graph becomes denser closer to its center.

the input image, where each entry  $M(i, j)$  contains the label value of the component to which the pixel  $p(i, j)$  belongs.

In the fourth step, a region-adjacency graph  $G = (V, E)$  is constructed based on  $M$ . Each vertex  $v_i \in V$  represents a region and its index corresponds to its label. The edges in  $E$  connect pairs of adjacent regions. To reduce the number of edges we use a  $4 \times 4$  neighborhood. Figure 3h shows the graph-based representation of the image presented in Fig. 3a, and Fig. 5 shows an example of a typical graph. Note that  $G$  is an undirected, simple graph that does not contain any isolated vertex, since all components are connected at least to the background image.

Each ES cell is represented in  $G$  by a simple path  $S$ , whose vertices are in ascending order. A simple path is defined as a sequence of distinct vertices such that from each vertex there is an edge to the next vertex in the sequence. Thus, in the fifth step,  $V$  is evaluated iteratively checking only for the vertices with degree smaller than three. Such vertices are classified either as a new simple path or as a component of a simple path that was detected previously. Figures 6 and 8b present the simple paths detected for the images shown in Figs 3a and 8a, respectively. For more details about the graph-mining process applied, please see [14].

Although this method works well in most cases, as Figs 7a and 7b illustrate, it is prone to errors when many cells contain more than one bright point (see Fig. 7c). Steps 1 to 5 assume that a cell has only one bright

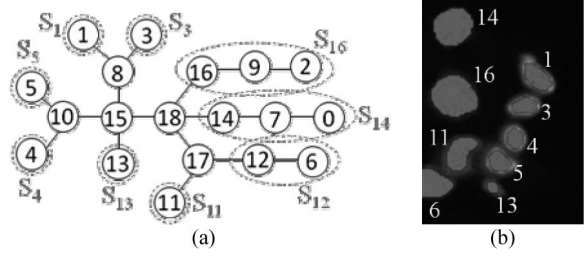


Fig. 6. Outcome of the graph mining process: (a) the simple paths detected, represented by the red dashed lines; and (b) the components (in red) of each simple path in the input image with the corresponding simple path numbers (in yellow).

point and the luminance decreases monotonically from this point to the boundary of the cell. However, due to biological phenomena such as DNA condensation and pyknotic nuclei [23], this assumption is not always true and step 6 is required when the image presents this situation.

To reduce the number of false positives, i.e., elements that are wrongly classified as cells, step 6 performs a hierarchical graph clustering [33]. This step merges the simple paths that represent a same cell into clusters (supersets). These paths are identified using the Euclidean distance and graph topology. We assume that, if a set of simple paths represents the same cell, they should have a common neighbor, as illustrated in Figure 8b (simple paths  $S_5$ ,  $S_6$  and  $S_7$ , for example). To facilitate the description of the algorithm, consider the follows definitions:

- the **distance** between two simple paths  $S_i$  and  $S_j$  is given by  $d_E(c_i, c_j)$ , where  $c_i$  and  $c_j$  are the central points of the bounding boxes of the regions that have the highest labels in  $S_i$  and  $S_j$ , respectively;
- the **neighborhood** of a simple path  $S_i$  is defined as the vertices neighboring the vertices of  $S_i$  that are not in  $S_i$ ;
- two simple paths  $S_i$  and  $S_j$  are **neighbors** if there is at least one edge connecting a vertex of  $S_i$  to a vertex of  $S_j$ ;
- a **superset** is a set of vertices made up of simple paths and additional vertices.

The basis of the clustering algorithm is that two simple paths  $S_i$  and  $S_j$  represent the same cell if  $d_E(c_i, c_j) < \lambda$ , where  $\lambda$  is half of the diameter of an average cell measured from the input image. If  $c_i$  and  $c_j$  represent distinct cells, the bright points in their interior may be superimposed and, as a consequence, these cells will be counted as one by biologists.

To implement this step, consider the following algorithm. Given a graph  $G$  and the list  $L = \{S_1, S_2, \dots,$

Table 1

Our database is divided into seven image groups, and the corresponding input parameters used are: the value of the Gaussian radius ( $\sigma$ ), the parameter ( $x$ ) used to calculate the threshold, the interval size ( $\varepsilon$ ), and half of the diameter of an average cell ( $\lambda$ )

Database			Parameters			
Group	N. of images	Image type	$\sigma$	$x$	$\varepsilon$	$\lambda$
1	69	EB cryosections with an acceptable level of noise	2	0.3	8	12
2	23	EB cryosections with strong presence of noise	3	0.3	8	12
3	32	EB cell migration with a $40 \times$ zoom	2	0.3	16	30
4	17	EB cell migration with a $20 \times$ zoom	2	0.3	16	15
5	66	mES cell colonies under MEF with a $20 \times$ zoom	2	0.3	8	15
6	12	mES cell colonies under MEF with a $10 \times$ zoom	2	0.3	8	7
7	15	neurosphere images	2	0.3	32	10

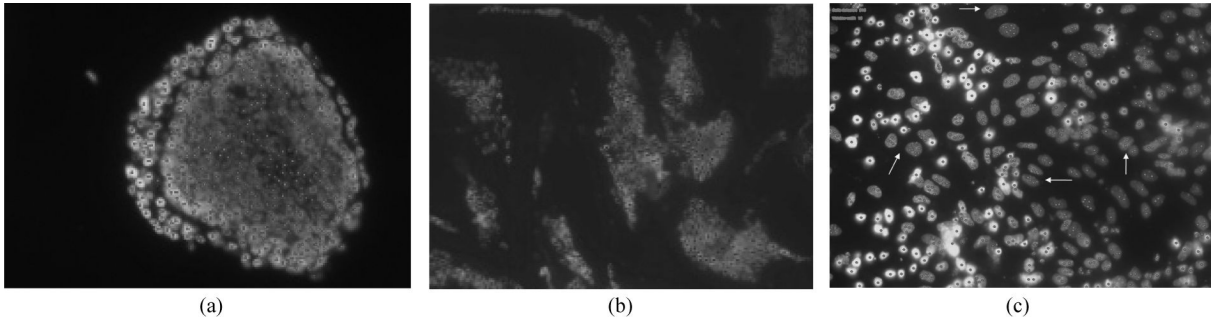


Fig. 7. Results of the graph mining algorithm: the points in blue (b) and red (a and c) represent the cells detected. (a) EB cryosection image; (b) image of mES cell colonies under MEF with a  $20 \times$  zoom; and (c) image of EB cell migration with a  $40 \times$  zoom where the yellow arrows indicate some cells that have more than one bright point and as a consequence were detected more than once.

$S_n$  of simple paths detected through the mining process, in order to group the simple paths that represent a same cell into clusters, do the following:

1. Group the simple paths of  $L$  that have a common neighbor into sets of vertices.
2. For each set, merge those paths that represent the same cell ( $d_E < \lambda$ ) into supersets. If all simple paths of a given set are merged and the common vertex does not represent the background, add this vertex to the superset. Simple paths that are not merged in this step become a superset.
3. Evaluate the neighborhood of each superset and add the vertices that: a) do not belong to any other superset; b) are not neighbors of any other superset; and c) do not represent the background image.
4. Merge the supersets that represent the same cell (neighboring supersets or the ones that have a common neighbor, and  $d_E < \lambda$ ).
5. Repeat steps 3 and 4 until no supersets can be merged and no vertex can be added to some superset.

The result is a collection of supersets (clusters) in the graph, each representing one cell. These steps are

depicted as the transitions from Figs 8b to 8i. Figure 8j shows the outcome of the clustering algorithm applied to the input image.

## 5. Experimental results and discussion

In this section, we present a numerical evaluation of the proposed method. Although cell counting is a well known problem, we are not aware of any other method that handles several types of pluripotent stem cells in the same microscopy image. For this reason, we include here a comparative study with the flooding-based watershed algorithm [12], which is a classical algorithm used for image segmentation.

In order to compare the quality of the methods, we measured precision ( $P$ ), recall ( $R$ ) and F-measure ( $F$ ), which are defined as:  $P = tp/(tp + fp)$ ,  $R = tp/(tp + fn)$ , and  $F = (2*P*R)/(P + R)$ , where  $tp$  (true positive) represents the number of items correctly labeled as cells,  $fp$  (false positive) represents the items incorrectly classified as cells, and  $fn$  (false negative) represents items that were not classified as cells but should have been.

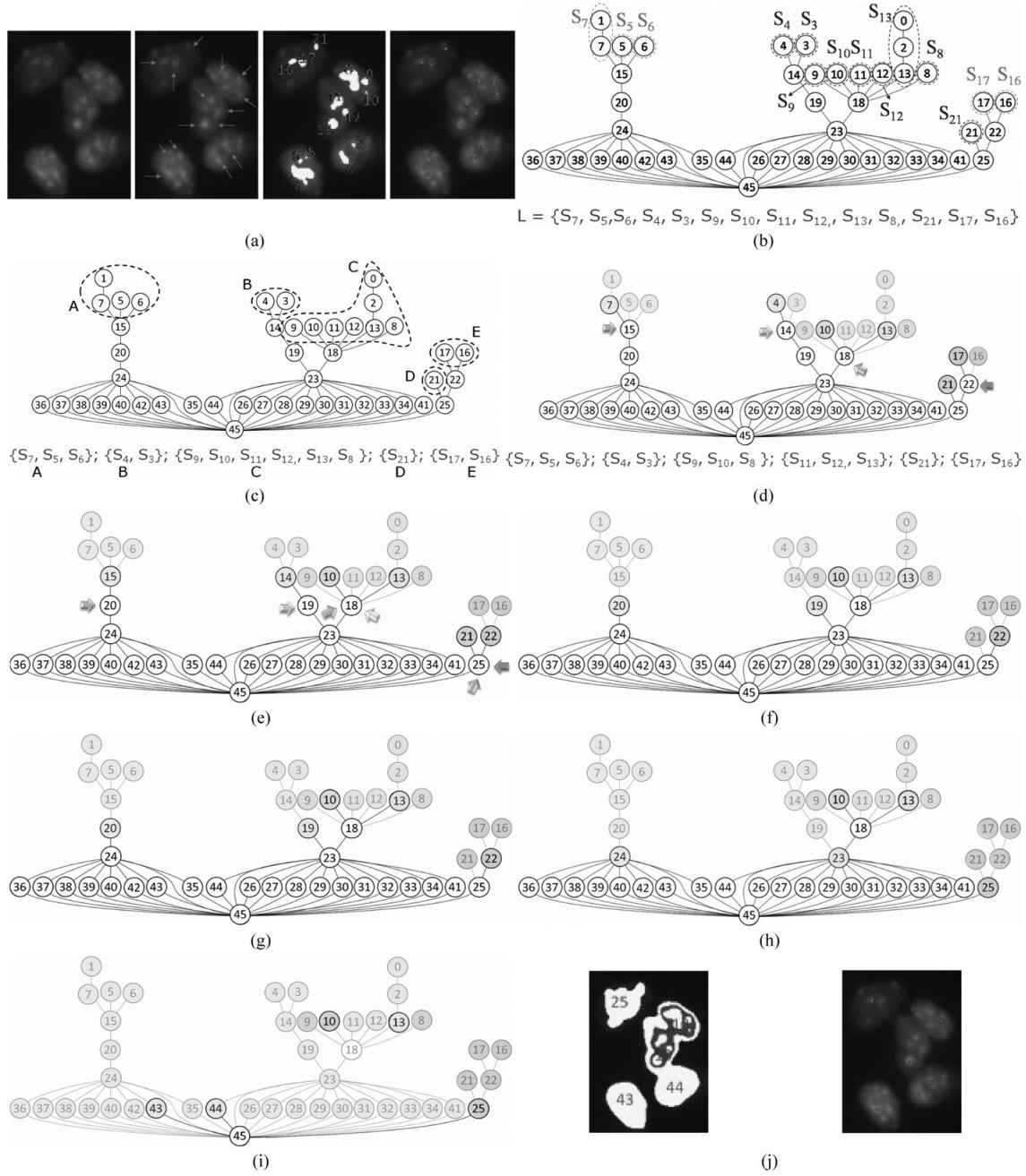


Fig. 8. Result of graph mining and outcomes of each step of the graph clustering algorithm: (a) input image (the pink arrows indicate the brightest points) and result of the mining process (the yellow regions represent the simple paths with the highest vertex indices in red; the red dots represent the cells detected up to this point); (b) input of the clustering algorithm: graph  $G$  and list  $L$  (the simple paths  $S_i$  detected in the mining process are identified by dashed lines); (c) outcome of step 1, where the dashed lines represent the sets of vertices; (d) partial result of step 2: note that set  $C$  became two supersets (represented in red and green), and the common neighbors, which are indicated by the colored arrows, were still not evaluated; (e) final outcome of step 2: the supersets are represented by different colors, and the neighborhood of each superset is indicated by the colored arrows; (f) outcome of step 3: note that the vertices 18 and 25 were not added; (g) outcome of step 4: the supersets represented in pink and blue were merged; (h) partial outcome of step 5: as a result of a new iteration of step 3, the vertices 24, 23 and 25 were added to the supersets represented in orange, blue and pink, respectively; (i) final outcome of step 5: a collection of supersets, each one representing a cell; and (j) result of the clustering algorithm applied to the input image.



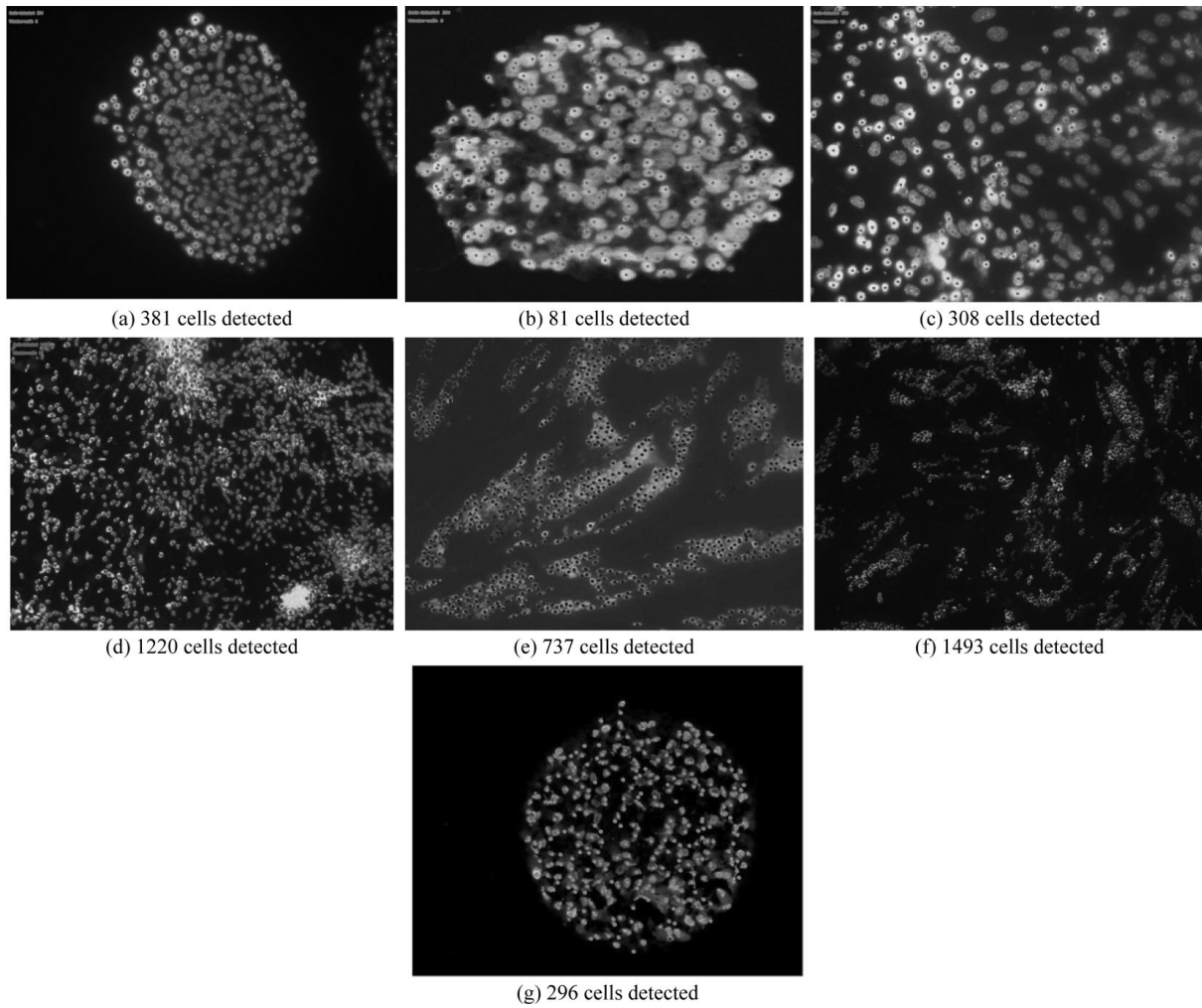


Fig. 9. Results of our method: (a) and (b) show images of EB cryosections with acceptable (group 1) and high (group 2) level of noise, respectively; (c) and (d) present images of EB cell migration with a  $40\times$  and  $20\times$  zoom (groups 3 and 4), respectively; (e) and (f) show images of mES colonies under MEF with a  $20\times$  and  $10\times$  zoom (groups 5 and 6), respectively; and (g) presents a neurosphere image. The dots in red (a to d, and g) and blue (e and f) represent the cells detected. These results were achieved by applying the graph clustering algorithm in (a), (b), (c) and (d), and using only graph mining for (c), (d) and (g). For these images we obtained an F-measure of 94.07%, 91.82%, 96.95%, 96.71%, 92.96%, 95.29%, and 96.05%, respectively.

A database with 234 images similar to those shown in Section 2 was constructed and divided into seven groups as illustrated in Table 1. Groups 1 to 4 are the same data presented in our previous work [13]. The values for the input parameters presented in Table 1 were obtained through experimental tests.

All images processed by our method were checked by specialists from the Institute of Biomedical Sciences at UFRJ. They identified cells that were not counted (false negatives) and artifacts that were incorrectly classified as cells (false positives). Thus, the measures were calculated for each image and then an average was estimated for all images. The computed results are

presented in Table 2, and Fig. 9 shows some images processed by our method. The results for groups 1, 2 and 3 were obtained including the optional step (graph clustering); groups 4 to 7 did not include this step, as will be discussed below.

In the case of images of EB cell migration with a  $20\times$  zoom (group 4) and images of mES cell colonies under MEF with  $20\times$  and  $10\times$  zoom (groups 5 and 6, respectively), due to the zoom factor the cells present in these images are very small and are displayed with only one bright point. If the clustering algorithm were applied, it would group some simple paths that represent different cells, and some cells that were detected cor-

Table 2

Experimental results of our method. All numbers are average values over all images. The last column indicates whether the graph-clustering algorithm was used

	Precision (%)	Recall (%)	F-measure (%)	Clust Alg
Group 1	96.29	93.13	94.60	✓
Group 2	96.96	91.48	94.08	✓
Groups 1 and 2	96.47	92.68	94.46	✓
Group 3	89.74	83.70	86.09	✓
Group 4	95.97	93.44	94.63	
Group 5	94.69	85.28	89.55	
Group 6	97.82	80.39	87.88	
Group 7	94.71	90.95	92.67	

Table 3

Sets representing the main groups. The first column indicates the sets and the second indicates the corresponding groups they represent. The third column describes the number of images and their type

Sets	Groups	Composed of
1	1 and 2	20 images of EB cryosections
2	3	12 images of EB cell migration (40 × zoom)
3	4	6 images of EB cell migration (20 × zoom)
4	5	14 images of mES cell colonies (20 × zoom)
5	6	5 images of mES cell colonies (10 × zoom)
6	7	7 images of neurospheres

rectly would be lost. Thus, for these types of images, the optional step of our method should not be applied. Using only the first five steps, our method achieved an average F-measure of 93.87%, 83.20% and 87.78% for these groups, respectively.

Although the neurosphere images (group 7) were captured with a 40 × zoom, due to biological factors these cells display only one bright point when visualized through fluorescence microscopy. Therefore, as explained previously, the clustering algorithm is not necessary. For these images, we obtained an average precision, recall and F-measure of 94.71%, 90.95% and 92.67%, respectively.

In the case of EB cryosections (groups 1 and 2) and images of EB cell migration with a 40 × zoom (group 3), due to the large zoom factor these cells are displayed with better resolution and, as a consequence, present additional bright points in their interior. Therefore, for these images, we used the sixth step as described in the previous section.

By adding the graph-clustering algorithm to the process, the precision, recall and F-measure of EB cryosection images was improved by 2.49%, 0.64% and 1.58%, respectively. Regarding images of EB cell migration (group 3), the precision of the method was improved by 22.41%. However, some cells that were very close (with a distance smaller than  $\lambda$ ) were detected as a single one, increasing the number of false negatives.

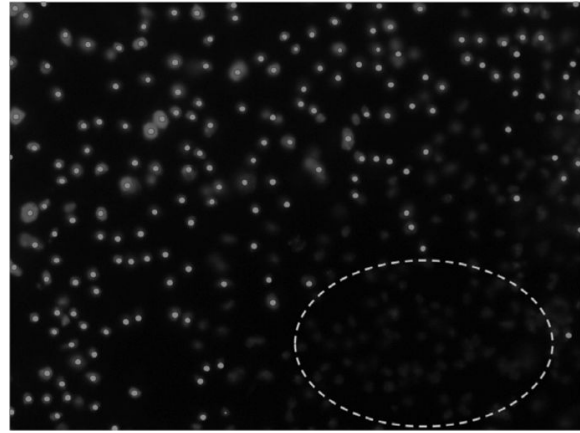


Fig. 10. A captured image with low contrast: the red dots represent the detected cells and the yellow circle indicates a region in the image where no cells were detected.

Nevertheless, the F-measure increased from 77.83% to 86.09% for these images. Table 4 presents the obtained results with and without the application of the clustering algorithm.

As demonstrated here, the proposed method provides satisfactory results, which can be improved further by applying the graph-clustering algorithm. However, it is still prone to errors when the contrast among cells or between the cells and the background is very low. When this happens, during the histogram partition step these cells can fall in the same luminance class that contains the background image, or even disappear during the background segmentation process, and then fail to be detected. As a consequence, they are not detected. In spite of this issue, the numbers presented in Table 2 are in agreement with human expert results. Moreover, according to the expert biologists, our method is sufficiently accurate for biological practices.

We have also developed a free software application with user interface called Embryonic Stem Cell Counter (ESCC), which uses the methodology proposed here to automatically calculate the number of ES cells in images like the ones described in Section 2. It was implemented in Java Language 6.0 using the development tool Eclipse 3.2. This software is already in use at the Institute of Biomedical Sciences at UFRJ, Brazil, and can be downloaded freely at <http://esccl.inf.puc-rio.br/>. Using this software, the biologists were able to reduce the average counting time from 15 minutes to 6.2 seconds per image. Furthermore, since the algorithm always uses the same criteria, it eliminates subjectivity. The software can provide reliable results for a large-scale experiment in hours, versus months of tedious

Table 4  
Comparison between the methods. All numbers are average values over all images. The first column represents the sets

S E T S	Proposed method						Watershed Algorithm		
	Without graph clustering			With graph clustering					
	P	R	F1	P	R	F1	P	R	F1
	(%)			(%)			(%)		
1	93.57	93.65	93.55	95.82	94.03	94.86	62.80	97.94	76.34
2	62.69	94.21	74.42	95.51	89.45	92.23	34.36	98.12	50.21
3	96.48	95.67	96.05	97.14	84.96	90.62	76.75	97.65	85.86
4	96.05	88.99	92.29	95.27	78.85	86.03	82.01	95.59	88.21
5	97.70	77.78	86.07	97.68	77.08	85.59	83.69	93.77	88.19
6	96.58	90.79	93.55	95.86	84.25	89.49	68.91	97.96	80.86

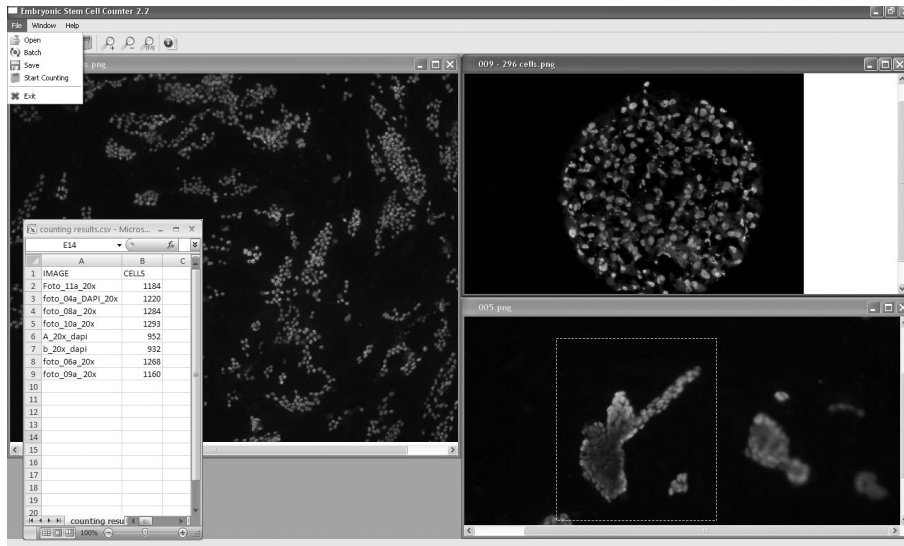


Fig. 11. Embryonic Stem Cell Counter software (ESCC), designed for counting ES cells in fluorescence microscopy images.

visual inspection. Figure 11 shows a screenshot of ESCC.

### 5.1. Comparison with the watershed algorithm

In order to compare the method proposed here with the flooding-based watershed algorithm [12], random images were selected from each group. We constructed six sets, each one representing the corresponding main group, as shown in Table 3. Figure 1 shows examples of captured images from each set.

The images were preprocessed by applying the same Gaussian filter and background segmentation described previously. Then, the images were processed using the ImageJ plugin provided by the Biomedical Imaging Group – EPFL [4], which implements the watershed algorithm by flooding, as proposed by Meyer [12].

The evaluation was performed visually by the authors based on examples of correct counts provided by biologists. Table 4 presents the average precision, recall and F-measure for the sets described above, and Figure 12 compares the results achieved using our method and those from the watershed algorithm for the images of each set. Figure 13 presents some images processed by both methods.

Comparing the results, we can note that our algorithm performs better than the watershed algorithm for almost all images, as illustrated in Fig. 12. In addition, it can be parameterized easily for each image group.

In the case of images of EB cryosections (set 1), EB cell migration with  $40 \times$  and  $20 \times$  zoom (sets 2 and 3, respectively), mES cell colonies under MEF with a  $20 \times$  zoom (set 4), and neurospheres (set 6), the proposed method is, on average, 31% more precise than the watershed algorithm. Moreover, it achieved an

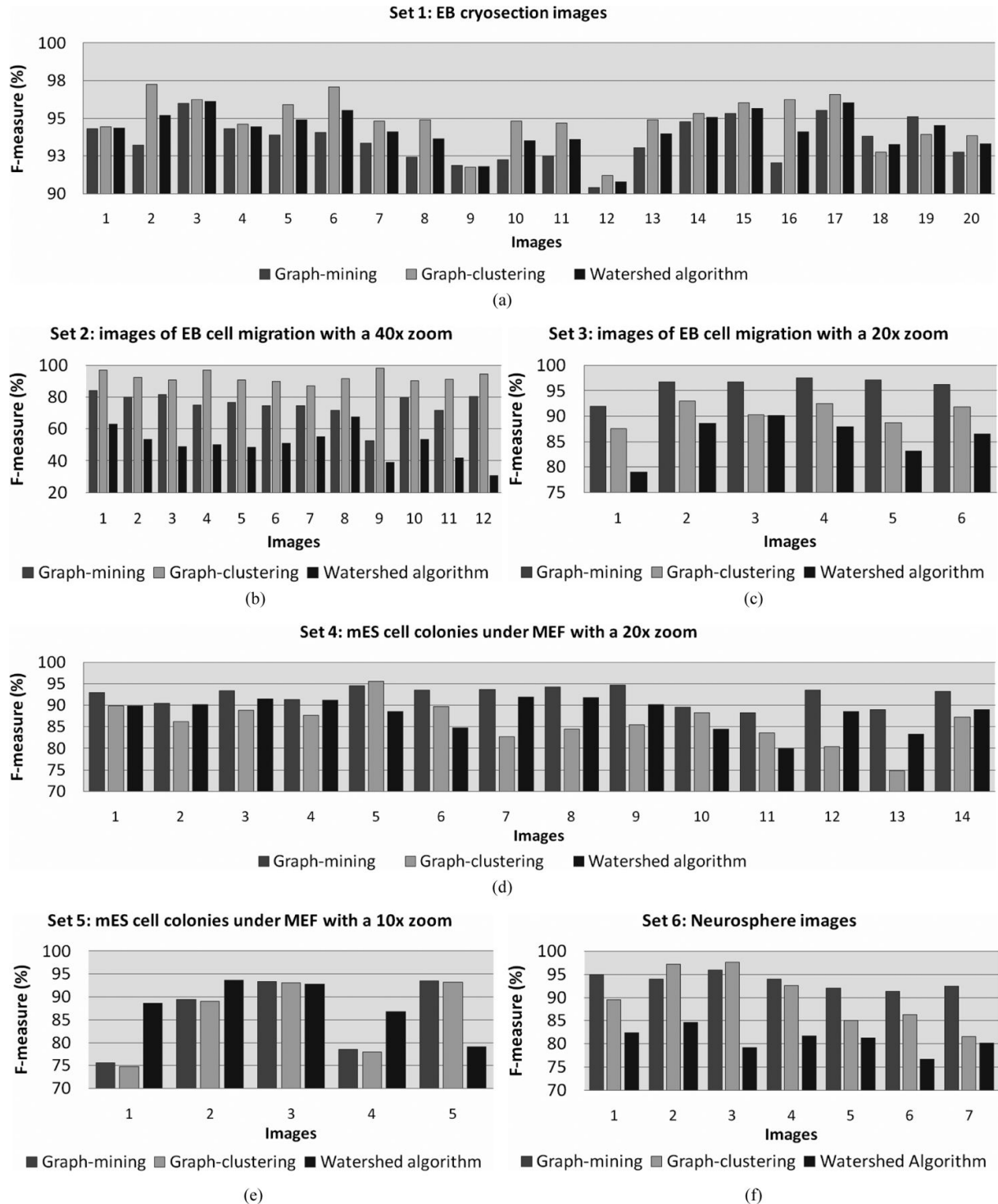


Fig. 12. Comparison among the original method, its improved version, and the watershed algorithm: (a) EB cryosection images; (b) and (c) images of EB cell migration with  $40\times$  and  $20\times$  zoom, respectively; (d) and (e) mES cell colonies under MEF with  $20\times$  and  $10\times$  zoom, respectively; and (f) neurosphere images. All images were evaluated by the authors based on examples of correct counts provided by biologists.

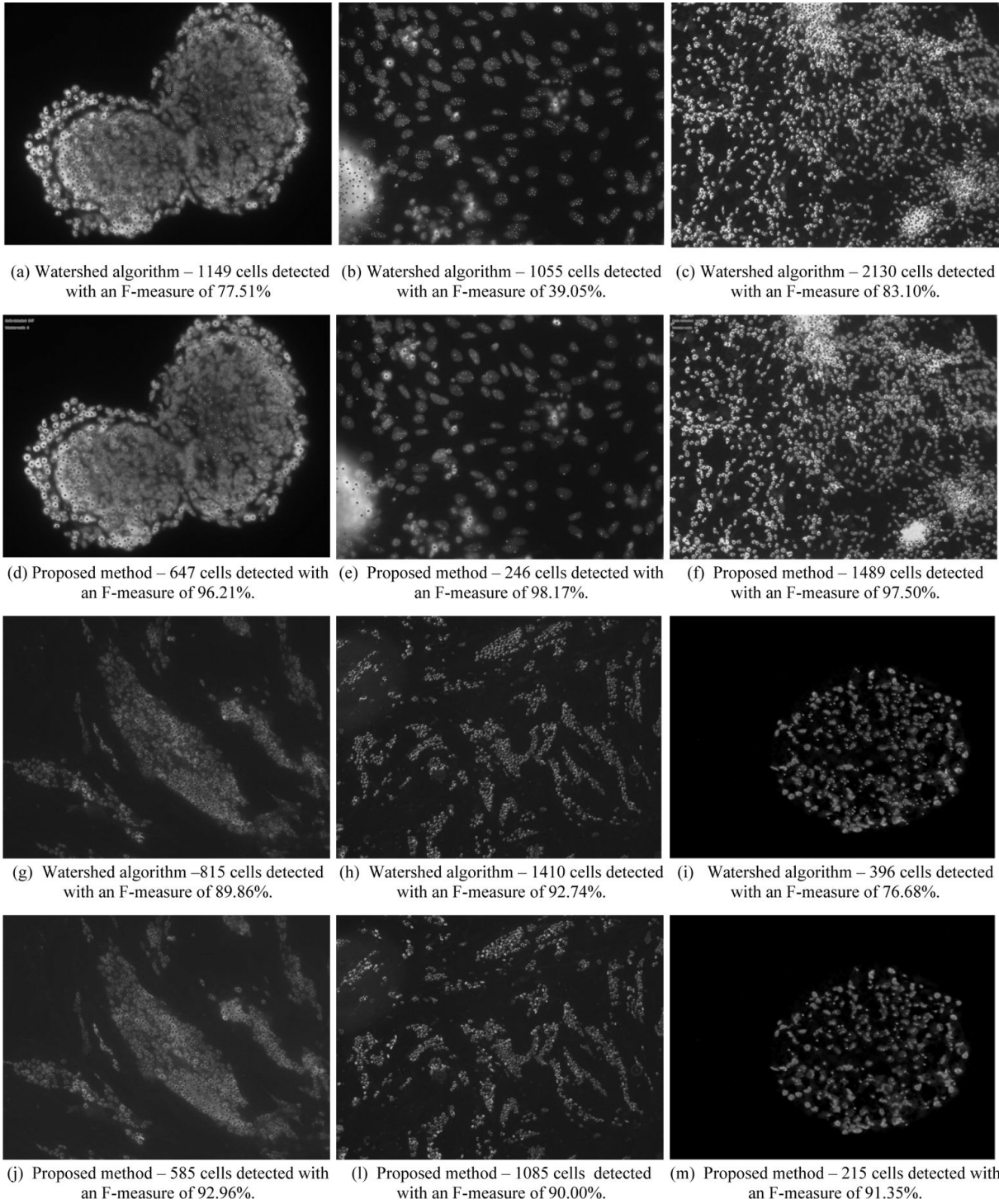


Fig. 13. Results of the proposed method and the watershed algorithm: (a) and (d) compare the results for EB cryosection images; (b) and (e) for EB cell migration with a  $40 \times$  zoom; (c) and (f) for EB cell migration with a  $20 \times$  zoom; (g) and (j) for mES cell colonies under MEF with a  $20 \times$  zoom; (h) and (l) for mES cell colonies under MEF with a  $10 \times$  zoom; and (i) and (m) for neurosphere images. The dots in red and in blue represent the detected cells.

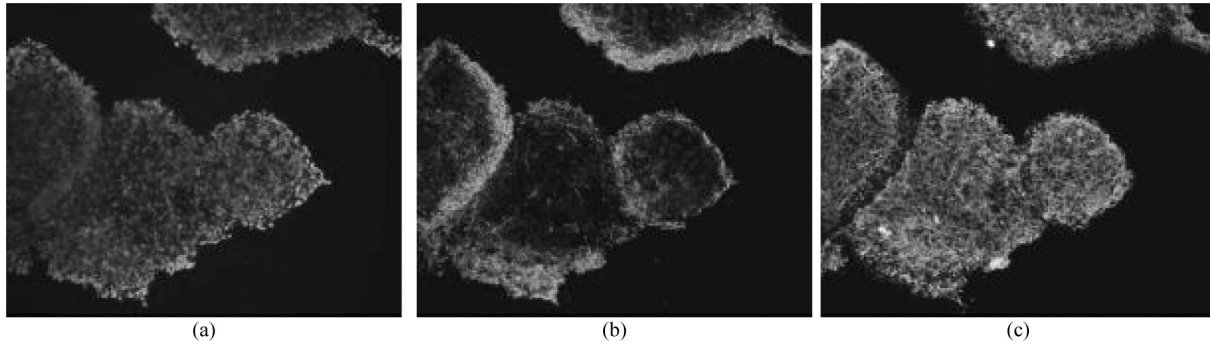


Fig. 14. Example of an image stained with DAPI and two different cell markers: (a) DAPI marker – stains all cells; (b)  $\beta$ -III tubulin – a neuron-specific marker; and (c) GFAP – a glial marker. In this image, it is possible to identify the percentage of neurons and glial cells.

average F-measure of over 90% against 76% obtained by watershed.

Regarding images of mES cell colonies with a  $10 \times$  zoom (set 5), we can see that the watershed algorithm generates better results. However, the difference between F-measures is under 2.2%. Watershed obtained average precision, recall and F-measure of 83.69%, 93.77% and 88.19%, respectively, against 97.70%, 77.78% and 86.07% through our method. At this zoom, these cells are tiny and their contrast is usually low, so our method does not detect as many cells as the watershed algorithm. On the other hand, in order to achieve these results, the watershed flooding level needs to be tuned for each image, while our method is easily parameterized for each image group.

Generally, the watershed algorithm provides satisfactory results if the cells do not present strong overlapping and do not contain more than one very bright point. However, if the cells are heavily clustered (e.g., Fig. 12a) or contain many bright points (e.g., Fig. 12b), its results are considerably different from our method. Moreover, in order to obtain satisfactory results with the watershed algorithm, we have to assess the outcome of each flooding level and choose the one which best fits the current image.

## 6. Conclusion and future work

Interdisciplinary research has great potential for innovation. In this paper, we presented new results of our automatic ES cell detection and counting method, which was designed for images of EB cryosections and ES cell migration. We have tested this method extensively with a large database, which includes two new image types: mES cell colonies under MEF, and neurospheres. Specialists from the Institute of Biomed-

ical Sciences at UFRJ university in Brazil validated the results. Our method achieved an average F-measure above 90%.

Comparing our method with the watershed algorithm proposed by Meyer [12], we could see that our methodology is, on average, 31% more precise for images of EB cryosections, ES cell migration, mES colonies under MEF with a  $20 \times$  zoom, and neurospheres, and it achieved an average F-measure above 90%, against 76% obtained by watershed. For images of mES colonies under MEF with a  $10 \times$  zoom, the watershed algorithm generated slightly better results. However, it requires tuning the flooding level for each image, while our method is automatic for images with the same differentiation protocols.

We have also developed a free software application – Embryonic Stem Cell Counting (ESCC) – which implements the methodology described in this article for the automatic counting of ES cells in fluorescence microscopy images. To further support our method, we are making our implementation and the images shown in this work public. The ESCC software is already being used at the Institute of Biomedical Sciences at UFRJ, Brazil, and is becoming a useful tool, since it ensures the pinpoint accuracy required by the procedures.

Future work includes extending the methodology presented here to deal with ES cells under MEF stained with DAPI. Although our method is currently able to detect these cells, it is not capable of distinguishing between ES cells and MEF.

The authors also intend to study the use of other metrics, such as max or group average distance, in the graph-clustering algorithm. Although the current method yields satisfactory results using the Euclidean distance, if necessary it could be easily adapted to other metrics.

Furthermore, we intend to extend the method to handle other cell markers, such as Map2, Nestin, Sox and Tuj1, thus developing the current software to calculate the percentage of differentiated, undifferentiated and dead cells automatically. Figure 13 shows an example of an ES cell image stained with DAPI and two different cell markers.

## Acknowledgments

Thanks are due to Aristófares C. e Silva for his most valuable assistance and to the team of collaborators of the Institute of Biomedical Sciences at UFRJ, Brazil. The team helped us validate the algorithm and contributed with discussions about the research hypothesis. The authors are supported by CAPES and CNPq.

## References

- [1] A. Garrido and N. PeHrez de la Blanca, Applying deformable templates for cell image segmentation, *Pattern Recognition* **33**(5) (2000), 821–832.
- [2] A. Korzynska, Automatic counting of neural stem cells growing in cultures, *Computer Recognition Systems* **2**(ASC 45) (2007), 604–612.
- [3] A. Niemisto, L. Hu, O. Yli-Harja, W. Zhang and I. Shmulevich, Quantification of *in vitro* cell invasion through image analysis, EMBS, pp. 1–5, 2004.
- [4] BioWatershed on Graylevel Images – ImageJ Plugin, Biomedical Imaging Group – EPFL Lausanne, <http://bigwww.epfl.ch/sage/soft/watershed/>, February 2008, last accesses 05/2010.
- [5] C. Liu, F. Li, Y. Zhang and H. Gu, Interactive Image Segmentation Based on Hierarchical Graph-Cut Optimization with Generic Shape Prior, in Proceedings of International Conference on Image Analysis and Recognition (ICIAR'09), LNCS 5627, pp. 201–210, 2009.
- [6] C. Restif, Segmentation and Evaluation of Fluorescence Microscopy Images, Thesis for the degree of Doctor of Philosophy, Oxford Brookes University, 2006.
- [7] C. Tang and E. Bengtsson, Segmentation and tracking of neural stem cell, in Proceedings of International Conference on Intelligent Computing (ICIC'05), pp. 851–859, 2005.
- [8] C. Zimmer, E. Labruière, V. Meas-Yedid, N. Guillén, and J.C. Olivo-Marin, Improving active contours for segmentation and tracking of motile cells in videomicroscopy, in Proceedings of 16th International Conference on Pattern Recognition, pp. 286–289, 2002.
- [9] D. Anoraganingrum, Cell segmentation with median filter and mathematical morphology operation, in Proceedings of IEEE International Conference on Image Analysis and Processing (ICIAP '99), pp. 1043–1046, 1999.
- [10] E. Glory, A. Faure, V. Meas-Yedid, F. Cloppet, Ch. Pinset, G. Stamon and J.-Ch. Olivo-Marin, A quantification tool to analyse stained cell cultures, in Proceedings of International Conference on Image Analysis and Recognition (ICIAR' 04), pp. 84–91, 2004.
- [11] F. Ambriz-Colin, M. Torres-Cisneros and J.G. Avina-Cervantes, Detection of biological cells in phasecontrast microscopy images, in Proceedings of the Fifth Mexican International Conference on Artificial Intelligence (MICA I '06), pp. 68–77, 2006.
- [12] F. Meyer, Un algorithme optimal pour la ligne de partage des eaux, in Dans 8me congrs de reconnaissance des formes et intelligence artificielle, Vol. 2, pp. 847–857, 1991.
- [13] G. Faustino, M. Gattass, C.J.P. de Lucena, Priscila B. Campos and S. Rehen, Improved Automatic ES Cells Counting Method in Fluorescence Microscopy Images, in Proceedings of International Conference on theoretical, experimental and applied signal and image processing techniques and systems (IWSSIP'10), pp. 296–299, 2010.
- [14] G. Faustino, M. Gattass, S. Rehen and C.J.P. de Lucena, Automatic embryonic stem cells detection and counting method in fluorescence microscopy images, in Proceedings of IEEE International Symposium on Biomedical Imaging (ISBI'09), pp. 99–102, 2009.
- [15] H. Sheikh, Bin Zhu and E. Micheli-Tzanakou, Blood cell identification using neural networks, in IEEE Twenty-Second Annual Northeast Bioengineering Conference, pp. 119–120, 1996.
- [16] I. Moon and B. Javidi, Three-dimensional identification of stem cells by computational holographic imaging, *J R Soc Interface* **4**(13) (2007), 305–313.
- [17] J. Logan, K. Edwards and N. Saunders, Real-Time PCR: Current Technology and Applications, Caister Academic Press, 2009.
- [18] J. Pathak, T.M. Johnson and C.G. Chute, A Supervised Learning Approach to Biological Question Answering, *Integrated Computer-Aided Engineering* **16**(3) (2009), 271–281.
- [19] J. Pathak, T.M. Johnson and C.G. Chute, Modular Ontology Techniques and their Applications in the Biomedical Domain, *Integrated Computer-Aided Engineering* **16**(3) (2009), 225–242.
- [20] K. Althoff, J. Degerman, and T. Gustavsson, Combined segmentation and tracking of neural stem cells, in Proceedings of Scandinavian Conference on Image Analysis (SCIA), pp. 282–291, 2005.
- [21] K. Takahashi, K. Tanabe, M. Ohnuki, M. Narita, T. Ichisaka, K. Tomoda and S. Yamanaka, Induction of pluripotent stem cells from adult human fibroblasts by defined factors, *Cell* **5**(131) (2007), 861–872.
- [22] M. Rizzi, M. D'Aloia and B. Castagnolo, Computer aided detection of microcalcifications in digital mammograms adopting a wavelet decomposition, *Integrated Computer-Aided Engineering* **16** (2009), 91–103.
- [23] M. Sell, Stem Cells Handbook, Human Press, 2003.
- [24] N.N. Kachouie, P. Fieguth and E. Jervis, Stem cell localization: a deconvolution problem, in Proceedings of 29th Annual International Conference of the IEEE Engineering in Medicine and Biology Society (EMBS 2007), pp. 5525–5528, 2007.
- [25] N.N. Kachouie, L.J. Lee and P. Fieguth, A probabilistic living cell segmentation model, *Proceedings of IEEE International Conference on Image Processing* **1** (2005), 1137–1140.
- [26] N.N. Kachouie, P. Fieguth, J. Ramunas and E. Jervis, Probabilistic model-based cell tracking, *International Journal of Biomedical Imaging* (2006), 1–10.
- [27] O. Schmitt and M. Hasse, Morphological multiscale decomposition of connected regions with emphasis on cell clusters, *Computer Vision and Image Understanding* **113** (2009), 188–201.

- [28] P. Bamford, Segmentation of cell images with an application to cervical cancer screening, PhD thesis, University of Queensland, 1999.
- [29] Q. Zheng, B.K. Milthorpe and A.S. Jones, Direct neural network application for automated cell recognition, *Cytometry A* **57**(1) (2004), 1–9.
- [30] R. Hedjam and M. Mignotte, A hierarchical graph-based markovian clustering approach for the unsupervised segmentation of textured color images, in 16th IEEE International Conference on Image Processing (ICIP'09), pp. 1365–1368, 2009.
- [31] R.J. Qureshi, J.-Y. Ramel and H. Cardot, Graph based shapes representation and recognition, in Graph-Based Representations in Pattern Recognition- GbRPR, Springer Berlin / Heidelberg, 2007, p. 4960.
- [32] R.T.K. Lin, H.J. Dai, Y.Y. Bow, R.T.H. Tsai and M.Y. Day, Using Conditional Random Fields for Result Identification in Biomedical Abstracts, *Integrated Computer-Aided Engineering* **16**(4) (2009), 339–352.
- [33] S. E. Schaeffer, Graph Clustering, *Computer Science Review* **1**(1) (2007), 27–64.
- [34] S. Sergent-Tanguy, C. Chagneau, I. Neveu and P. Naveilhan, Fluorescent activated cell sorting (facs): a rapid and reliable method to estimate the number of neurons in a mixed population, *J of Neuro Meth* **129**(1) (2003), 73–79.
- [35] S. Shiotani, T. Fukuda, F. Arai, N. Takeuchi, K. Sasaki and T. Kinoshita, Cell recognition by image processing: (recognition of dead or living plant cells by neural network), *JSME* **37** (1994), 202–208.
- [36] S. Vicente, V. Kolmogorov and C. Rother, Graph cut based image segmentation with connectivity priors, in Proceedings of IEEE Conference on Computer Vision and Pattern Recognition (CVPR'08), pp. 1–8, 2008.
- [37] T. Markiewicz, S. Osowski, J. Patera and W. Kozłowski, Image processing for accurate cell recognition and count on histologic slides, Intl, *Academy of Cytology* **28**(5) (2006), 281–291.
- [38] T. Spencer, J.A. Olson, K.C. Mchardy, P.R. Sharp and J.V. Forrester, An image-processing strategy for the segmentation and quantification of microaneurysms in fluorescein angiograms of the ocular fundu, *Computers and Biomedical Researches* **29** (1996), 284–302.
- [39] X. Long, W.L. Cleveland, and Y.L. Yao, Effective automatic recognition of cultured cells in bright field images using fisher's linear discriminant preprocessing, *Image and Vision Computing* **23**(13) (2005), 1203–1213.
- [40] Y. Liu and C. Pomalaza-Ráez, On-Chip Body Posture Detection for Medical Care Applications Using Low-Cost CMOS Cameras, *Integrated Computer-Aided Engineering* **17**(1) (2010), 3–13.
- [41] Y. Liu and C. Pomalaza-Ráez, On-Chip Body Posture Detection for Medical Care Applications Using Low-Cost CMOS Cameras, *Integrated Computer-Aided Engineering* **17**(1) (2010), 3–13.